X-ray spectromicroscopy of single NiO antiferromagnetic nanoparticles

A. I. Figueroa,[1,2*] C. Moya, [1,2] M. X. Aribó,[1] J. Ara,[1] M. García del Muro,[1,2] A. Kleibert,[3] S. Valencia,[4] A. Labarta, [1,2] X. Batlle[1,2] and A. Fraile Rodríguez[1,2*]

[1] Departament de Física de la Matèria Condensada, Universitat de Barcelona, Martí i Franquès 1, 08028 Barcelona, Spain

[2] Institut de Nanociència i Nanotecnologia (IN2UB), Universitat de Barcelona, 08028 Barcelona, Spain

[3] Swiss Light Source, Paul Scherrer Institut, 5232 Villigen PSI, Switzerland

[4] Helmholtz-Zentrum Berlin für Materialien und Energie, D-12489 Berlin, Germany

Corresponding authors: aifigueroa@ub.edu, arantxa.fraile@ub.edu

Abstract

The chemical and magnetic properties of NiO nanoparticles (NP) have been studied with single-particle sensitivity by means of synchrotron-based, polarization dependent X-ray absorption spectroscopy using photoemission electron microscopy around the Ni $L_{3,2}$ edges. Three samples of NP in a size range of 40-120 nm were synthesized by thermal decomposition and subsequent calcination processes. The analysis of the local X-ray absorption spectra of tens of individual NP indicates a strong dependence of their Ni oxidation state with the calcination protocol of each sample. Additional electron-microscopy-based images and spectra of few individual NP as well as other standard macroscopic data are in very good agreement with these experimental findings. These results showcase the relevance of combining standard and advanced single-particle studies to gain further insight into the understanding and control of electronic and magnetic phenomena at the nanoscale.

Keywords: X-ray absorption spectroscopy, X-ray photoemission electron microscopy, antiferromagnetic nanoparticles, single-particle characterization, Nickel oxide.

1. Introduction

Nanoscale magnets show unusual magnetic behavior when compared to their bulk counterpart, mostly due to surface/interface and finite size effects, including symmetry breaking, modified electronic environment, and magnetic correlations and interactions.[1] The great potential of those emergent nanoscale properties for their application in diverse areas has attracted thorough investigations for decades. Nevertheless, even with the advanced and forefront characterization techniques currently available to study magnetic nanoparticles (NP), neither a quantitative understanding nor a control of their size-dependent properties has been fully achieved. Most experiments focus on integrated measurements of large ensembles, and thus, yield averages of the NP properties that are strongly dependent on their morphology (size and shape distributions), chemical composition (oxidation states), crystallinity, magnetic interactions, and/or defect configuration, which could mask more complex single-particle properties within the ensembles. It is, therefore, crucial to count with probes of the magnetism of individual NP.

Few experimental techniques are nowadays available, and suitable, to study the magnetic structure in isolated or interacting NP, such as microSQUID magnetometry and electron holography.[2] Recent advances on X-ray magnetic spectromicroscopy techniques at synchrotron radiation facilities have established X-ray photoemission electron microscopy (PEEM) as one of the best suited techniques to investigate the magnetic properties and chemical composition of individual NP under ultrahigh vacuum conditions.[3-5] This is a non-invasive, element-specific technique providing quantitative information about the chemical composition, electronic structure, and magnetism of individual NP.[6-11] Being a full-field imaging technique, X-ray PEEM probes simultaneously several individual NP in large ensembles, giving direct insight into the distribution of the magnetic properties in typical samples. Furthermore, X-ray PEEM offers a great advantage over other experimental techniques, which is the possibility of not only examining the properties of ferromagnetically ordered systems, but also accessing magnetic information of antiferromagnetically ordered ones. Thus, we have exploited this aspect by analyzing, with single-particle sensitivity, the chemical and magnetic properties of three samples of NiO NP in a size range of 40-120 nm, synthesized by thermal decomposition and subsequent calcination processes, focusing on the impact of the latter. The interest of studying NiO NP lies in their relevant physical features when compared to the bulk materials, such as charge-transfer effects and interesting antiferromagnetic (AF) spin structure.[12] By combining PEEM with X-ray magnetic linear dichroism (XMLD) around the Ni $L_{3,2}$ edges we access information about the AF order within individual NiO particles. Moreover, the magnetic and chemical properties of the NP were directly correlated with their structural characterization by combination of X-ray PEEM spectromicroscopy with atomic resolution transmission electron microscopy (TEM). This work highlights the importance of combining standard and advanced characterization techniques to delve into magnetic phenomena of AF NP, making a significant contribution to the field of nanomaterials and their applications.

2. Methods

2. 1. Preparation of the NiO NP

Three samples of NiO NP with sizes between 40 and 120 nm were prepared by thermal decomposition and subsequent calcination processes. Sample A was synthesized by a high-temperature decomposition method using 1 mmol of $Ni(acac)_2$, and 4 mmol of oleic acid in 5 ml of benzyl-ether, modifying a conventional synthesis method described elsewhere.[13] First, the reaction mixture was degassed at 100 ºC for 30 minutes. Then, argon gas was introduced, and the mixture was heated to 220 ºC with vigorous stirring for 120 minutes. After this, the solution was subjected to reflux at a rate of 9.5 ºC/min for 60 minutes. Upon completion of the reflux, the solution was cooled to room temperature and transferred to a centrifugation tube with a 3:1 mixture of acetone and toluene. The mixture was then centrifuged at 9000g to remove the organic residues. This washing process was repeated twice to ensure thorough cleaning. The resulting black solid was dried using compressed nitrogen gas and then redispersed in 5 ml of toluene. Finally, sample A was stored at 5 ºC until further thermal treatment.

Samples B and C were obtained from a two-step thermal treatment process performed on a fraction of sample A. A first portion was heated to 450ºC for 72 hours under atmospheric conditions, resulting in sample B. To produce sample C, an additional thermal treatment was applied on a portion of sample B, involving heating the sample to 700ºC for 72 hours in atmospheric conditions.

2.2. Structural and macroscopic magnetic characterization

Samples for TEM inspection were prepared by dropping 20 µL of a diluted suspension in toluene onto a carbon-coated Cu grid, followed by drying under vacuum conditions. TEM characterization was conducted using a JEOL JEM 2010F operating at a working voltage of 200 kV. Histograms of the size distribution of the samples were determined by measuring at least 300 particles with *ImageJ* software[14] and fitting the results to a log-normal probability distribution of the form:

$$P(D) = \frac{1}{S\sqrt{2\pi}D}\, e^{-\ln^2\left(\frac{D}{D_0}\right)/\left(2S^2\right)} \tag{1}$$

where D is the particle diameter, D_0 stands for the most probable value of D, and S is the standard deviation of the distribution of the logarithm of the reduced diameter D/D_0. D_0 and S were determined by fitting experimental histograms obtained from TEM data to Eq. 1.[15] The mean particle size D_{TEM} and the standard deviation σ of the diameter distribution were computed from Eq. 2 and Eq.3, respectively, as follows:

$$D_{TEM} = D_0\, e^{S^2/2} \tag{2}$$

$$\sigma = D_0\, e^{S^2/2\sqrt{e^{S^2}-1}} \tag{3}$$

Finally, the polydispersity index σ_{RSD} of the samples was estimated by dividing the standard deviation by the mean particle size $\sigma_{RSD} = \sigma/D_{TEM}$.

The chemical composition of individual particles was analyzed by electron energy loss spectroscopy (EELS), with a spatial resolution of approximately 1 nm. This analysis was performed with a JEOL JEM 2010F operating in scanning TEM mode.

The structural characterization of the samples was performed by combining high-resolution TEM (HRTEM) and selected area electron diffraction (SAED) analysis. The interplanar distances (d_{hkl}) were calculated using Gatan Microscopy Suite® software for HRTEM images,[16] while *ImageJ* graphical analysis was employed for SAED patterns.[14] The interplanar SAED distances were calculated by measuring the separation between the central spot and the diffraction spots and converting the reciprocal space distances into real space ones. These results were then compared to the pattern generated by the X'Pert High Score Plus software for bulk Ni and NiO compounds, referring to the Inorganic Crystal Structure Database entries for NiO (PDF#71-1179) and elemental Ni (PDF#00-001-1260).

Further characterization of the crystal structure was performed by X-ray diffraction (XRD) using a PANalytical X'Pert PRO MPD diffractometer with Cu Kα radiation (λ = 1.5418 Å), scanning 2θ from 4 to 120° with a step size of 0.026°, and measuring time of 200 seconds. The positions of the peaks were compared to the above-mentioned

Ni and NiO reference patterns and fitted to determine the crystallite size, D_{XRD}, by Rietveld analysis by the FullProf Suite software.[17]

The macroscopic characterization of the samples was performed by recording hysteresis loops at 5 K and 300 K, applying a maximum magnetic field of ±70 kOe with a Quantum Design MPMS XL SQUID magnetometer. These measurements yielded the magnetization at the maximum field (±70 kOe), M_{max}, the coercive field, H_c, and the remanent magnetization, M_r, which were computed as $H_c = ([H_c^+] + [H_c^-])/2$ and $M_r = (|M_r^+| + |M_r^-|)/2$, respectively, where H_c^+ and H_c^- are the intercept values of the hysteresis loop with the positive and negative sides of the H-axis and M_r^+ and M_r^- are analogous intercept values of the hysteresis loop with the M-axis.

2.3. X-ray spectromicroscopy of single NP

X-ray PEEM spectromicroscopy was performed in the PEEM station at the Surface/Interface: Microscopy (SIM) beamline of the Swiss Light Source, Paul Scherrer Institut, Switzerland[8] and at the SPEEM station of the UE49/PGMa beamline of the synchrotron radiation source BESSY II of the Helmholtz-Zentrum Berlin.[18] The base pressure of the microscopes was below 10^{-10} mbar and all experiments were carried out at room temperature around the Ni $L_{3,2}$ edges. The NiO samples for the PEEM experiments were prepared by drop-casting a dilute solution onto a silicon wafer with lithographic markers. Subsequently, a thin carbon film was deposited onto the substrate to reduce charging and enhance the signal-to-noise ratio of the NP in the PEEM measurements.

The X-ray PEEM technique provides a full-field magnified image of the emitted secondary photoelectrons[8] with a probing depth of a few nm at the Ni $L_{3,2}$ edges,[19] which allows for spatial mapping of the absorption of the particles. X-ray absorption spectroscopy (XAS) measurements consisted of recording sequences of PEEM images using vertically or horizontally linearly polarized light, by scanning the photon energy around the Ni $L_{3,2}$ edges. To extract the local, isotropic XAS spectra (sum of horizontal and vertical polarization) for individual particles, alignment between all images in the stack for every energy was performed with a routine of *ImageJ* software.[14] Despite efforts in applying the optimal correction in the alignment, drifts below two pixels in x- and y-axes were unavoidable due to the low elemental contrast between the particles and the background signal, even more pronounced for the smallest particles. Consequently, a particle-by-particle background correction was applied given the non-similar emission and absorption characteristics of the different background zones.

For the processing and analysis of the images, particles with boxes of different sizes that adapted to their dimension in order to get the biggest and cleanest signal possible were selected. A box is defined as a rectangular-shaped area in the image. Some astigmatism effects are present on the images as asymmetrical halos, which are more evident for the largest particles. Note that the lateral spatial resolution of X-ray PEEM is limited, on the order of 30 nm, so the box size may not refer to the actual size of the NP, but the apparent one, as the XAS just indicates the regions where the electrons are emitted. In sample A, a total of 100 particles were selected, whereas in samples B and C only around 10 or less were analyzed. The number of particles analyzed is still sufficient to hold conclusive results about their chemical composition, even more than in other single-particle measurements techniques, such as HRTEM or EELS, by which often only a few NP are probed.

XAS spectra arise from the absorbed X-rays by core electrons of Ni atoms in the NP and provides information about the oxidation states and local atomic structure around them. Local XAS spectra were obtained by extracting the mean intensity of each box for every energy and dividing it by the background signal. The background of every particle is measured with the same box dimensions at a neighboring area without particles. Further details of this process can be found in Refs. [9,10]. In samples B and C, the XAS local spectra showed a monotonically decaying absorption with increasing energy due to the small signal of the NP, current decay and self-irradiation effects, among other possible reasons. These artefacts are not unusual in XAS-based measurements and have been corrected with a polynomial fit of the background curve. Normalization of the XAS curves for sample A was performed by scaling conveniently to 0 at the pre-edge L_3 and to 1 at the post-edge L_2. Due to the slope correction performed for samples B and C, such a normalization procedure was not possible in this case.

To quantify the amount of metallic Ni and NiO present in selected individual particles for samples A and B, the local isotropic XAS spectra were fitted to a weighted linear combination of reference bulk spectra of Ni and NiO taken from Ref. [12]. Further details of the process on which this analysis is based are given in Refs. [9,10]. The XMLD signal was calculated as the difference between spectra taken with vertical and horizontal linearly polarized light. While not on the scope of the present work, XMLD also yields information of magnetic ordering, being especially useful to probe AF order, as it is sensitive to the AF spin axis orientation through its proportionality to the expectation value of the square of the atomic magnetic moment $\langle m^2 \rangle$ (see e.g., Refs. [12, 19]).

3. Results and discussion

Figure 1 depicts the overall structural properties of the samples obtained from TEM, which reveal two distinct particle morphologies depending on the thermal treatment. Sample A exhibits spherical particles with an average diameter of 36 nm and some faceting, suggesting preferential growth along the {111} and {220} planes. This is a common effect in oleic acid-assisted thermal decomposition for metal oxide materials containing cubic crystal structures like Ni or NiO.[20] On the contrary, sample C shows irregular, cluster-like structures with an average size of roughly 120 nm. This morphology suggests a coalescence process during thermal treatment probably due to the long period of exposition at the high temperature of 700 ºC. Note that sample B exhibits a morphology nearly identical to sample A, with an average size of about 33 nm, implying a negligible impact of the thermal treatment of this sample on the particle morphology. Histograms of the size distribution for all samples can be found in Fig. S1 of the Supplementary Information.

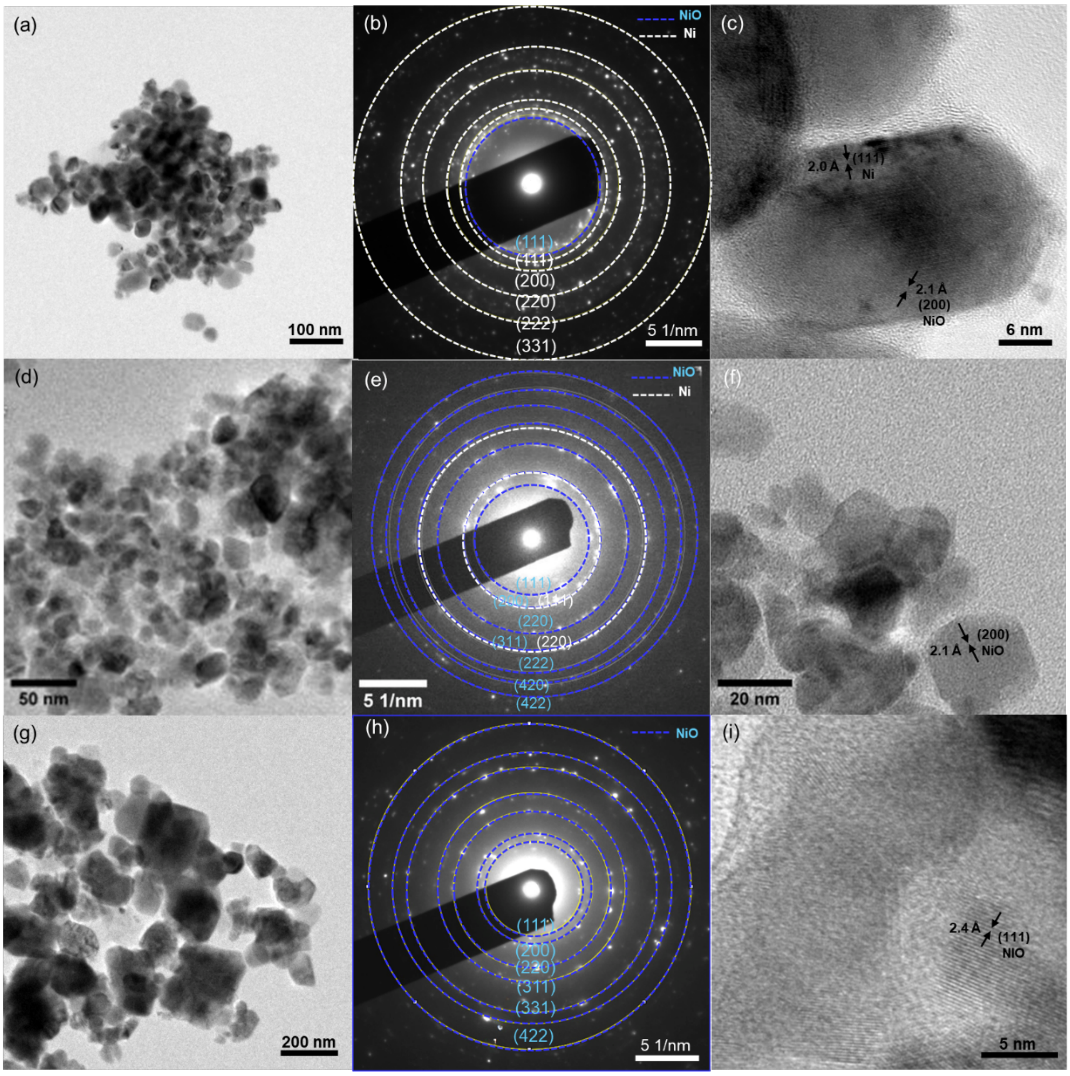

Figure 1. TEM characterization of samples A (top panel), B (middle panel), and C (bottom panel). (a), (d) and (g) Low-magnification TEM images showing agglomerates consisting of several tens of particles. (b), (e) and (h) Corresponding SAED patterns revealing the coexistence of Ni and NiO planes for samples A and B, and only interplanar distances typical of NiO for sample C. (c), (f) and (i) HRTEM images with detailed views of single particles and their crystallographic planes.

SAED analysis, shown in Fig. 1, suggests the presence of both Ni and NiO phases for samples A and B, whereas sample C exhibits only interplanar distances attributed to NiO. Interestingly, High-Angle Annular Dark Field (HDAAF) imaging of a few particles for samples A and C, depicted in Fig. 2, rules out the presence of core-shell structures. This observation is further supported by HRTEM analysis included in Fig. 1, which reveals that the samples contain particles with defective crystal quality and multiple crystal planes, but no evidence of core-shell nanostructures. These findings suggest that the particles are formed by different crystallographic domains of either Ni and/or NiO phases.

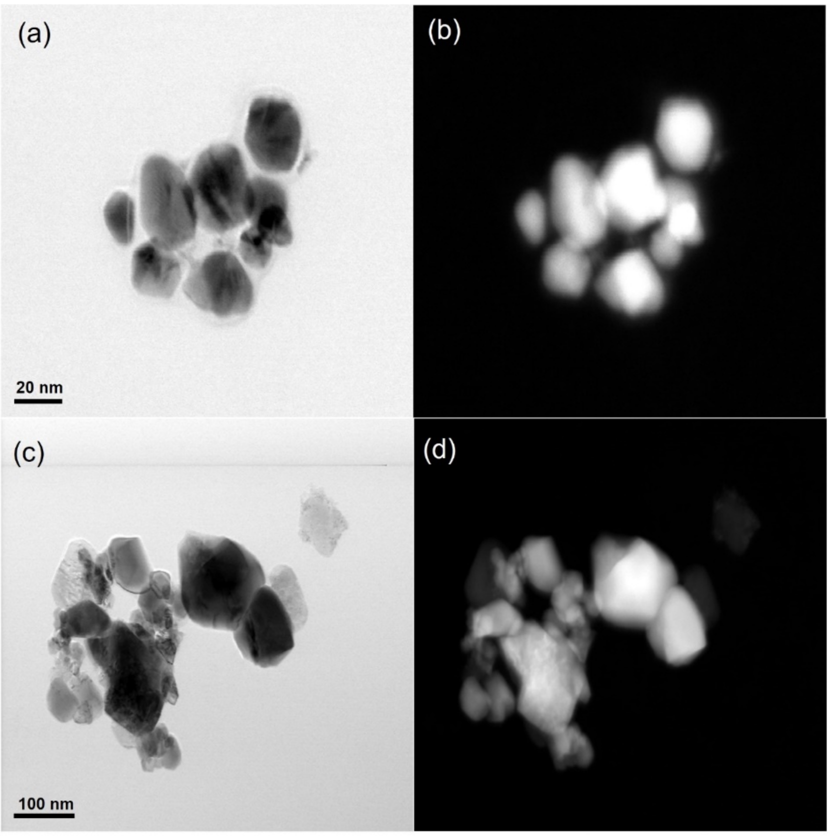

Figure 2. TEM and HAADF images of samples A (top panels) and C (bottom panels). (a) Bright field TEM image of sample A showing an agglomerate of 9 particles. (b) Corresponding HAADF image of sample A highlighting the uniform contrast of the particles. (c) Bright field TEM image of sample C displaying irregular, cluster-like structures. (d) Corresponding HAADF image of sample C. Notice the difference in scale bars in both cases, as NP in sample C are bigger than those in sample A.

To gain further insight into the atomic composition of sample A, EELS mapping of a few particles was performed, which is shown in Fig. 3. The compositional Ni and O maps display a homogenous distribution of both elements, with a % mass ratio of approximately 80% and 20% for Ni and O, respectively. This suggests that sample A is primarily formed of Ni particles containing a slight amount of oxygen.

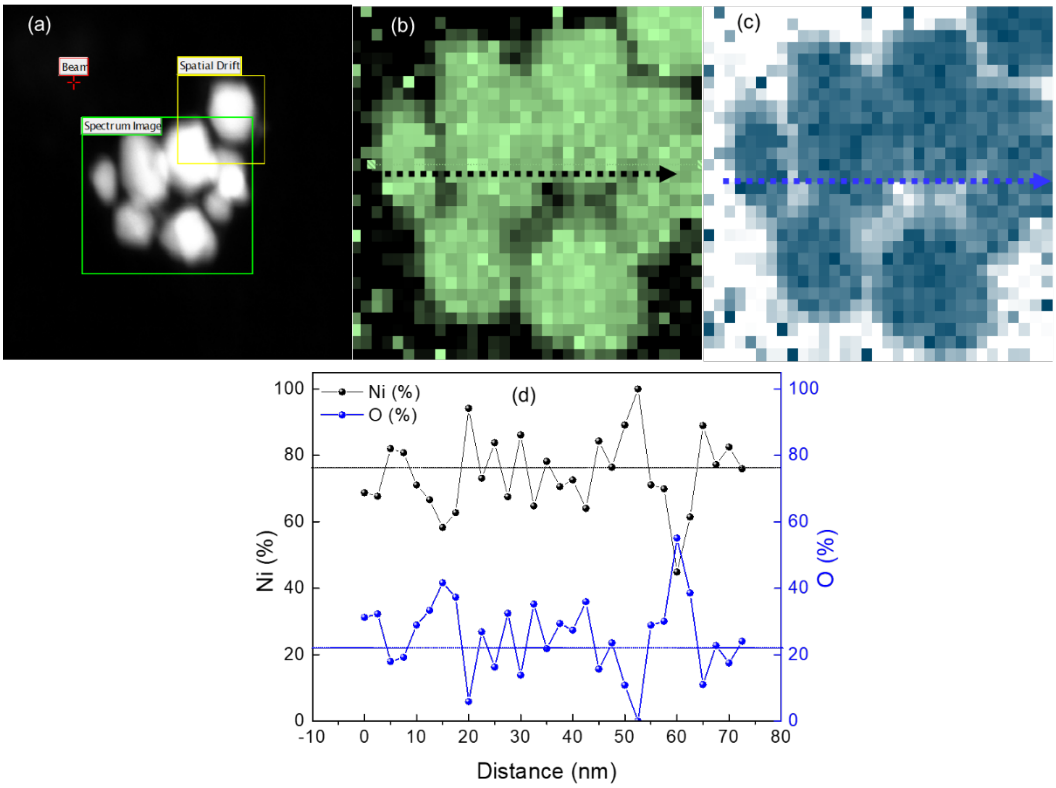

Figure 3. Compositional analysis of sample A using EELS mapping. (a) Spectrum image showing the spatial drift and beam positioning. (b) Ni L_3-edge relative composition map showing the distribution of Ni within the sample. (c) O *K*-edge relative composition map displaying the distribution of oxygen within the same area. (d) Line scan profile along the dashed line in images displayed in (a) and (b), showing the relative percentages of Ni (black line) and O (blue line) across the particle.

XRD analysis, shown in Fig. 4(a), reveals the presence of two phases in sample A, i.e., Ni and NiO, while sample C displays a pattern corresponding only to NiO, in good agreement with results from SAED. Besides, Rietveld refinement of the XRD data reveals a significant discrepancy between D_{XRD} and D_{TEM} for both samples, probably due to their polycrystalline nature, as observed with HRTEM. Quantitative compositional analysis of XRD data reveals a composition for sample A of approximately 85(5)% Ni with 15(5)% NiO, while sample C is entirely formed of NiO.

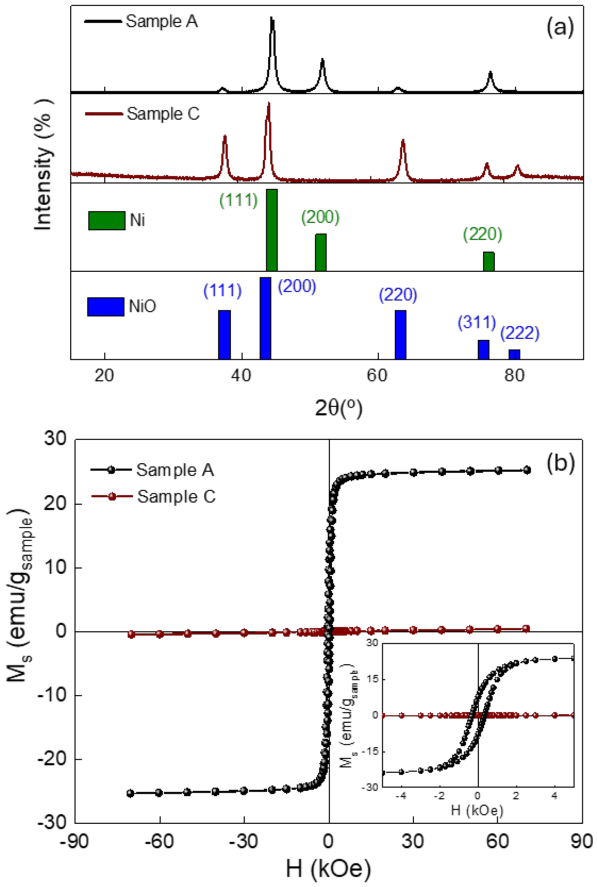

Figure 4. (a) XRD patterns of samples A and C, depicting the main diffraction peaks of Ni and NiO phases. (b) Hysteresis loops at 5 K within a field range of ±70 kOe for samples A and C. The inset details the low magnetic field region.

A summary of the main parameters extracted from the structural characterization for samples A and C are listed in Tab. 1. The structural properties of the samples have consequences in their magnetic behavior, as observed in the hysteresis loops recorded at 5 K for samples A and C, shown in Figure 4(b). Relevant magnetic parameters extracted from this macroscopic magnetometry are also listed in Tab. 1. The hysteresis loops of sample A exhibit typical ferromagnetic behavior, with a square-like curve indicative of ferromagnetic Ni.[21] The curve also shows a rapid magnetic response to the applied field, saturating at a field around 4.5 kOe (see inset in Fig. 4). Interestingly, $M_{max} = 25$ emu/g at 5 K is approximately half that of its bulk counterpart, suggesting the presence of crystal defects and/or antiferromagnetic phases within the particles.[8] Sample C, on the other hand, shows typical AF behavior [see red curve in Fig. 4(b)], characterized by a linear response to the applied magnetic field, and near-zero M_{max}, H_c, and ${}^{M_r}/_{M_{max}}$(indicating minimal net magnetization).

Table 1. Structural and magnetic parameters for samples A and C. $M_{max} = M(H = 70\text{ kOe})$.

Sample	**Morphology**	**D_{TEM} (nm) ± σ**	**σ_{RSD}**	**Main composition**	**D_{XRD} (nm) ± σ**	**M_{max} at 5K (emu/g)**	**M_r/M_{max} at 5K**	**H_c (5K) (kOe)**	**M_{max} at 300K (emu/g)**	**M_r/M_{max} at 300K**	**H_c (300K)**
A	Faceted round shape	36 ± 7	19	Ni	10 ± 1 (Ni), 3± 1 (NiO)	25 ± 1	0.32 ± 0.02	0.3 ± 0.1	22± 1	0.14 (2)	0.1 ± 0.05
C	irregular	117 ± 21	18	NiO	13 ± 2	0.4± 0.1	0	0	0.3± 0.1	0	0

The chemical composition and electronic structure of individual NP in the samples were analyzed by synchrotron-based, polarization-dependent soft X-ray absorption spectromicroscopy using PEEM. Representative examples of elemental-contrast X-ray PEEM images for all samples are shown in Fig. 5. Note that the differences in the overall image appearance between the three samples in Fig. 5 is an indication of the charging effects that challenge the analysis of the local spectra, as will be discussed below.

Representative examples of the isotropic, local XAS spectra obtained for selected particles on all samples are shown in Fig. 6. We identify the L_3 (~853 eV) and L_2 (~871 eV) edges of metallic Ni or NiO phases. A signature of the NiO phase is the edge splitting effect at the $L_{3,2}$ peaks, namely: at the Ni L_3, a shoulder (855.3 ± 0.1 eV) is observed, whereas the Ni L_2 edge exhibits a double peak feature (marked as A and B dashed lines in Fig. 6). Such a difference between the spectra for metallic Ni and NiO is due to the available final states in each case, being only two for elemental Ni, whereas multiplet effects yield more allowed transitions between the initial and final states in the case of NiO.

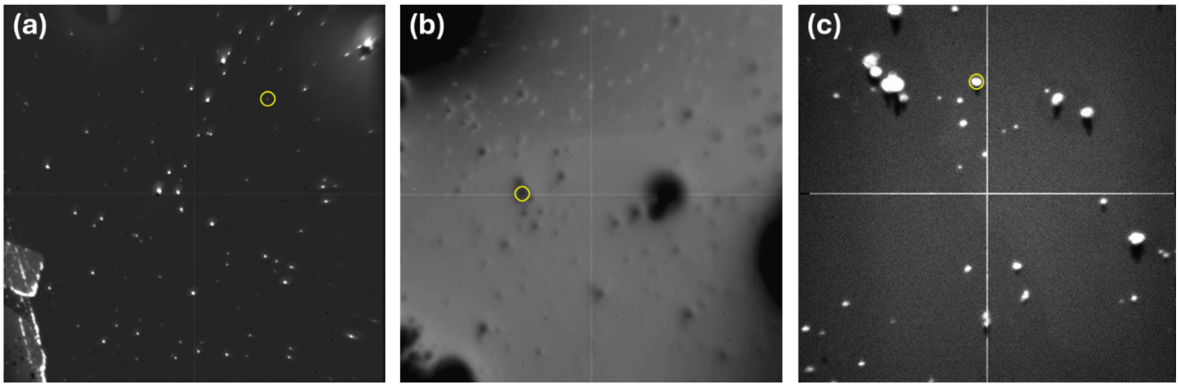

Figure 5. Elemental contrast X-ray PEEM images measured with linear polarization from sample (a) A, (b) B, and (c) C at the Ni L_3 edge, recorded with fields of view of 50 µm ((a) and (b)) and 20 µm, respectively). Yellow circles in all panels highlight some of the particles analyzed. Perpendicular lines on the images, which are more evident in (c), are artifacts of the detector used to record them.

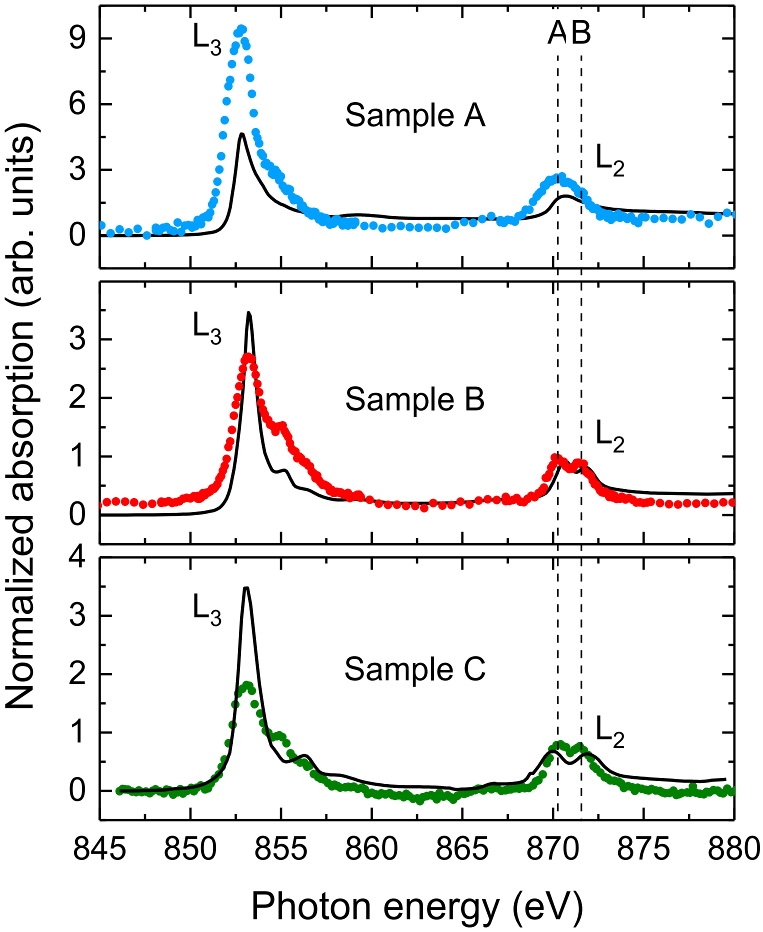

Figure 6. Normalized isotropic XAS spectra (symbols) from the selected particles highlighted in Fig. 5 of sample A (top panel), B (middle panel), and C (bottom panel) compared to the best-weighted fits from the Ni and NiO standards (solid black lines, Refs. [10, 19]). Dashed lines mark the position of peaks A and B around the L_2 edge, characteristic of NiO.

Considering the well-defined features observed at the Ni $L_{2,3}$ edges for metallic Ni and NiO, a criterion to distinguish each phase on the samples was defined, based on the L_2 splitting, the distances between the main peaks, and the ratio between them. The distance was computed using the position of peak A of the L_2 edge ($L_{2A,}$) instead of the average energy of L_{2A} and peak B (L_{2B}), as the latter was barely noticeable for most particles. Besides, the position of $L_{2A,}$ is fixed and very similar for both metallic Ni and NiO, thus it is a reliable reference photon energy value. We obtained from the standard spectra a distance of 17.4 ± 0.3 eV for NiO and 17.8 ± 0.2 eV for Ni.

From this analysis, particles of sample A resulted to be rather pure Ni, with 90% to 100% Ni, with an uncertainty of around 5%. This result is in very good agreement with the structural characterization performed on this sample by TEM, SAED, EELS, and XRD described above. Despite the presence of a small shoulder in L_3, as is typical of NiO, it was clear there was little oxide content due to the non-edge-splitting at the L_2 edge, as observed in Fig. 6. Nevertheless, XAS spectra for some particles in this sample exhibited a small splitting at the L_2. This, together with the apparent absence of the Ni 6 eV satellite feature, which was a common feature in all of our spectra, point towards the presence of some oxide phase. The mean distance between L_3 and L_{2A} for those particles was 17.3 ± 0.4 eV, which was compatible with the presence of both Ni and NiO phases. Therefore, our results suggest sample A is composed mostly of metallic Ni particles, with other NP with varying Ni/NiO composition, in agreement with what was observed by HRTEM and SAED.

Samples B and C turned out to be more oxidized, as evidenced by the shape of L_2 peak, as observed in Fig. 6. In this case, the intensity of the L_3 peak and the L_3:L_{2A} ratio is lower than expected, likely due to charging effects.[22] The mean distance between peaks was 17.4 ± 0.4, which is compatible with both phases. As these spectra had to be corrected for the decaying absorption with energy, the flat areas at the pre-edge L_3, the post-edge L_2, and between these two edges may be artificially enhanced and thus, do not fit so well to the reference spectra at these zones. Charging effects in the sample could also lead to higher intensity values, like in the L_3 shoulder. Despite this, we focused our interpretation on the L_2 shape and concluded that particles in sample B had between 15% and 30% of metallic Ni, with an uncertainty of 12%. Fits for sample C reveal that, according to our criterion, particles are composed of pure NiO within an error bar of around 10%.

Notice that the fits and the sample spectra do not seem to match perfectly, which is more evident for sample A, mainly because of the height difference between the reference and the sample peaks. This does not affect our analysis, since here we only focus on relative differences in spectral shape and proportionality, and not on quantifying the number of 2*p* to 3*d* transitions associated with the X-ray absorption process.

The XMLD signal was obtained by subtracting the signals of the two different polarization stacks. In this case, the background signal was measured with boxes of different shapes and sizes and located at various distances from the particle, as to improve the spectral quality for each polarization. XMLD results for selected particles on all samples are shown in Fig. 7. Although there are some hints of a dichroic signal in all cases, no apparent correlation with the amount of NiO in the sample was found. Whereas the isotropic XAS analysis indicated a predominance of the NiO phase for samples B and C, the resulting XMLD spectra were highly influenced by current decay and energy-dependent charging effects. In addition, the polynomial correction of the XAS spectra described above was not always successful as some of the spectra could not be properly normalized. All these issues resulted in noticeable noise and broadening of the XMLD signal for all particles analyzed, therefore, XMLD results are not conclusive.

It is important to remark that the low signal in all these analyzed NP have a very small signal-to-noise ratio, difficult to process and normalize properly. Moreover, we must bear in mind that the expected XMLD signal for these NP is very small, as the one for bulk NiO is <10%.[23] On top of that, we cannot rule out the possible existence of groups of nanocrystal grains with different AF axis orientations yielding an averaged signal where information about AF ordering would be hidden.

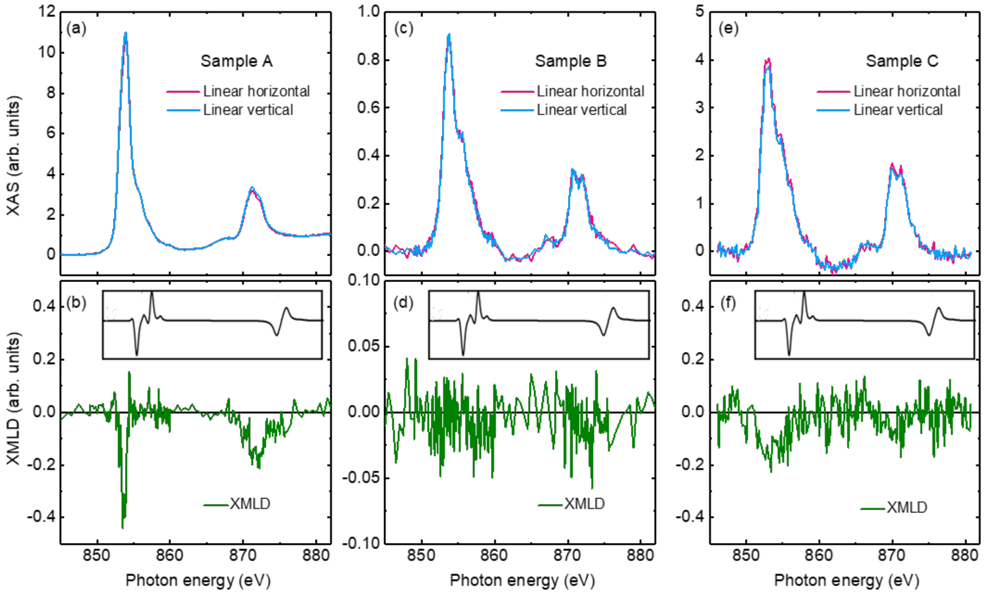

Figure 7. Comparison of XAS spectra ((a), (c) and (e)) with both linear polarizations, together with the resulting XMLD ((b), (d) and (f)), as obtained by subtracting the polarized signals, for the selected particles highlighted in Fig. 5 for samples A (a), B (b), and C(c), respectively. Insets display the expected XMLD signal for reference NiO thin films, as reported in Ref. [23].

To overcome the latter issue, further analysis could comprise XMLD-PEEM measurements with increased data statistics at larger magnifications, different orientations of the X-ray linear polarization vector, and a systematic azimuthal sample angular dependence, so that different AF spin easy axis orientations between individual NiO NP would be probed.

CONCLUSIONS

We have performed a thorough analysis of the chemical and magnetic properties of individual NiO NP of about 40-120 nm in size, from three different samples, prepared by wet chemical methods. Standard electron-microscopy-based techniques of (HR)TEM, SAED and EELS, macroscopic XRD and SQUID magnetometry were combined with advanced single-particle characterization by synchrotron-based X-ray spectromicroscopy using PEEM to gain relevant information on the oxidation state, crystal phases, and magnetic order in the samples. These analyses evidence a strong dependence of the oxidation state of the individual NP with the oxidation protocol of each sample: while sample A shows a prevalence of the metallic Ni phase, samples B and C show a predominance of the NiO phase. Obtaining unambiguous XMLD spectra would require improvements in data quality.

ACKNOWLEDGMENTS

The financial support from the Spanish MICIIN (grant numbers PGC2018-097789-B-I00, PID2021-127397NB-I00), Catalan AGAUR (Groups of Excellence 2021SGR00328), and the European Union FEDER funds are greatly recognized. The authors thank the Helmholtz-Zentrum Berlin für Materialien und Energie and the Swiss Light Source (SLS), Paul Scherrer Institut for the allocation of synchrotron radiation beamtime. CM acknowledges the funding support from the University of Barcelona and the Spanish Ministry of Universities under the program Maria Zambrano Program founded by the European Union Next Generation-EU/PRTR and the Beatriu de Pinós fellowship program with the number 2022 BP 00243. The author AIF is a Serra Húnter fellow. AIF expresses her deepest gratitude to Prof. Juan Bartolomé for his constant support ever since he was her PhD supervisor in Zaragoza, and highlights that his guidance and inspiration have been a guiding light in her career. XB recalls that he met Prof. Juan Bartolomé for the first time back in July 1987 at the *Laboratoire de Cristallographie* (‘*Cristallo’)* at CNRS-Grenoble. XB had just completed his Degree in Physics at the University of Barcelona, while Juan was already an extraordinary scientist who excelled, among others, in neutron diffraction, which was the PhD subject of XB at the Institute Laue-Langevin. Later, they met many times and enjoyed both a number of discussions about solid state physics and a long-standing friendship.

REFERENCES

[1] X. Batlle, C. Moya, M. Escoda-Torroella, O. Iglesias, A. Fraile Rodríguez, A. Labarta. Magnetic nanoparticles: From the nanostructure to the physical properties, J. Magn. Magn. Mater. 543, 168594 (2022)

[2] D.S. Schmool, H. Kachkachi, in Single-Particle Phenomena in Magnetic Nanostructures (Chap. 4), Solid State Physics, vol. 66, ed. by R.E. Camley, R.L. Stamps (Academic Press), pp. 301 – 423 (2015)

[3] A. Kleibert, Magnetism of Individual Nanoparticles Probed by X-Ray Photoemission Electron Microscopy. In: D. Peddis, S. Laureti, D. Fiorani (eds). New Trends in Nanoparticle Magnetism. Springer Series in Materials Science, vol 308. Springer, Cham. (2021)

[4] E. Bauer, *Surface Microscopy with Low Energy Electrons.* Springer, New York. (2014)

[5] C.A.F. Vaz, A. Kleibert, M. El Kazzi, in *Nanoscale XPEEM Spectromicroscopy 21st Century Nanoscience–A Handbook: Advanced Analytical Methods and Intrumentation*, Vol. 3, ed. By D.S. Klaus. CRC Press, Taylor & Francis Group, Boca Raton, London, New York. (2020)

[6] A. Fraile Rodríguez, A. Kleibert, J. Bansmann, A. Voitkans, L. J. Heyderman and F. Nolting, Phys. Rev. Lett., 104, 127201 (2010)

[7] F. Kronast, N. Friedenberger, K. Ollefs, S. Gliga, L. Tati-Bismath, R. Thies, A. Ney, R. Weber, C. Hassel, F. M. Romer, A. V. Trunova, C. Wirtz, R. Hertel, H. A. Dürr and M. Farle, Nano Lett., 11, 1710 (2011)

[8] L. Le Guyader, A. Kleibert, A. Fraile Rodríguez, S. El Moussaoui, A. Balan, M. Buzzi, J. Raabe and F. Nolting, J. Electron Spectrosc. Relat. Phenom., 2012, 185, 371. (2012)

[9] A. Fraile Rodríguez, C. Moya, M. Escoda-Torroella, A. Romero, A. Labarta and X. Batlle *J. Mater. Chem. C*, 6, 875-882 (2018)

[10] A. Fraile Rodríguez, A. Kleibert, J. Bansmann, and F. Nolting. Journal of Physics D: Applied Physics, 43(47):474006, (2010)

[11] J. Vijayakumar, T.M. Savchenko, D.M. Bracher, G. Lumbeeck, A. Béché, Nature communications 14 (1), 174 (2023)

[12] T. J. Regan, PhD dissertation, “X-ray absorption spectroscopy and microscopy study of ferro-and antiferromagnetic thin films, with applications to exchange anisotropy” (2001)

[13] X. He, W. Zhong, C.-T. Au, and Y. Du, Size dependence of the magnetic properties of Ni nanoparticles prepared by thermal decomposition method. Nanoparticle Res. Lett., 2013, **8**, 446. DOI: 10.1186/1556-276X-8-446.

[14] Rasband, W.S., ImageJ, U. S. National Institutes of Health, Bethesda, Maryland, USA, https://imagej.nih.gov/ij/, 1997-2022.

[15] M. Escoda-Torroella, C. Moya, A. Fraile Rodríguez, X. Batlle, A. Labarta, Selective Control over the Morphology and the Oxidation State of Iron Oxide Nanoparticles, Langmuir, 2021, **37**, 35-45. DOI: 10.1021/acs.langmuir.0c02221

[16] Gatan Microscopy Suite® software, Gatan, Inc., https://www.gatan.com/products/tem-analysis/gatan-microscopy-suite-software.

[17] J. Rodríguez-Carvajal, FullProf Suite, https://www.ill.eu/sites/fullprof/.

[18] F. Kronast, S. Valencia, J. Large-Scale Res. Facil. 2, A90 (2016)

[19] T. J. Regan, H. Ohldag, C. Stamm, F. Nolting, J. Lüning, J. Stöhr and R. L. White, Phys. Rev. B: Condens. Matter Mater. Phys., 64, 214422. (2001)

[20] S. Mourdikoudis, M. Menelaou, N. Fiuza-Maneiro, G. Zheng, S. Wei, J. Pérez-Juste, L. Polavarapu, and Z. Sofer, "Oleic acid/oleylamine ligand pair: a versatile combination in the synthesis of colloidal nanoparticles," Nanoscale Horiz., 2022, **7**, 941-1015, DOI: 10.1039/D2NH00111J.

[21] B. D. Cullity, C. D. Graham, Introduction to Magnetic Materials, 2nd ed., John Wiley & Sons, New York, (2009)

[22] B. Gilbert, R. Andres, P. Perfetti, G. Margaritondo, G. Rempfer, Gelsomina De Stasio Ultramicroscopy, 83:129– 139, (2000)

[23] Elke Arenholz, Gerrit van der Laan, and Frithjof Nolting. Applied Physics Letters, 93(16):162506, (2008)

Supporting Information

X-ray spectromicroscopy of single NiO antiferromagnetic nanoparticles

A. I. Figueroa,[1,2*] C. Moya, [1,2] M. X. Aribó,[1] J. Ara,[1] M. García del Muro,[1,2] A. Kleibert,[3] S. Valencia,[4] A. Labarta, [1,2] X. Batlle[1,2] and A. Fraile Rodríguez[1,2*]

[1] Departament de Física de la Matèria Condensada, Universitat de Barcelona, Martí i Franquès 1, 08028 Barcelona, Spain

[2] Institut de Nanociència i Nanotecnologia (IN2UB), Universitat de Barcelona, 08028 Barcelona, Spain

[3] Swiss Light Source, Paul Scherrer Institut, 5232 Villigen PSI, Switzerland

[4] Helmholtz-Zentrum Berlin für Materialien und Energie, D-12489 Berlin, Germany

Corresponding authors: aifigueroa@ub.edu, arantxa.fraile@ub.edu

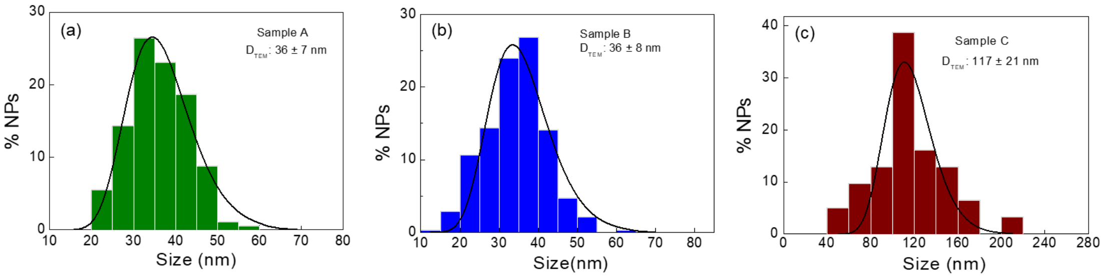

Figure S1. Size distributions for three different NiO samples measured by TEM. (a) Sample A, (b) sample B, and (c) Sample C. Solid black lines correspond to the respective fit to a normal distribution.